Chapter 10
Solar Radiation Maps

F. Díaz, G. Montero and L. Mazorra-Aguiar

Abstract Solar maps are very interesting tools to describe the characteristics of a region from the solar radiation point of view, and can be applied in atmospheric sciences and for energy engineering. To make them possible, a solar radiation numerical model is proposed. This one allows us to estimate radiation values in any point on earth. The model takes into account the terrain surface conditions and the cast shadows. The procedure uses 2-D adaptive triangles meshes built refining according to surface and albedo characteristics. Solar irradiance values are obtained for clear-sky conditions. Using clear sky index as a conversion factor, real-sky values are computed in terms of irradiance or irradiation with a desired time step. Finally, the solar radiation maps are obtained for all the domain.

10.1 Introduction

Solar radiation is important in several disciplines like agronomy, meteorology, medicine or engineering. Knowledge about solar radiation is essential for solar power generation and we all know the growing importance of these renewable energies. In literature, we can find mainly two kind of spatial solar radiation models:

- Those obtained through satellite observation [3]
- Those obtained using geometrical, physical and atmospheric conditions [1, 14, 23, 30, 31]

For the purpose of this chapter, we will focus on the second ones. These models take into account the interaction between radiation, Earth's atmosphere and terrain, in other words [30, 31]:

Felipe Díaz · Gustavo Montero · Luis Mazorra Aguiar
University Institute for Intelligent Systems and Numerical Applications in Engineering, University of Las Palmas de Gran Canaria, Edificio Central del Parque Tecnológico, Campus de Tafira, 35017, Las Palmas de Gran Canaria, Spain e-mail: felipe.diaz@ulpgc.es, gustavo.montero@ulpgc.es, luis.mazorra@ulpgc.es

1. Geometry of Earth (latitude, solar hour angle,...)
2. Terrain characteristics (surface inclination and orientation, elevation, albedo)
3. Atmospheric attenuation caused by gases, particles and clouds

The model with no clouds attenuation gives clear sky irradiance values. In the contrary, when attenuation is considered, computed values will be those of real sky irradiance. Some GIS based models [30, 31] are being used with an important computational cost when dealing with high accuracy. Starting from these ones, other numerical models have been developed with a lower computational cost [16, 5]. To reach this goal, the geographical domain is discretized using a 2-D adaptive mesh as described in Chapter 3 having as a reference the elevation, the inclination and the albedo of the terrain.

Another important issue to be considered is the shadowing effect that appears over a surface. Many researchers like Zakšek et al. [33] or Niewienda et al. [21] who proposes a geometrical shading coefficient to compute the effect of cast shadows, have studied this geometrical problem. As a result of the use of a regular grid, a high computational cost is obtained. Other researchers [8] do not consider solid surfaces so that higher density of sample points are needed. Recently, new approaches [6] for computing shadows have been developed.

10.2 Terrain and shadows modelling

10.2.1 Terrain mesh

The problem of computing solar radiation over the earth's surface begins with the discretization of the terrain. So, firstly we need to define a geographical domain where computations will be done. As said above in this book, we have faced the problem on complex terrains. In Chapter 3 the process to build the meshes for the terrain has been explained. An adaptive method for mesh refinement and derefinement can be applied using two different parameters, one for orography and another for albedo. Different meshing strategies may be used as can be seen in Chapter 3.

As grid examples, we present several domains where we have applied some computations explained in this chapter. In Figure 10.1, an adaptive mesh for Gran Canaria Island is shown. On the other hand, Figure 10.2 shows a mesh for the Tatra Mountains between Poland and Slovakia. Both are fine meshes that describe quite well the orography. However, for solar radiation purposes, coarser meshes can be used. In fact, for Gran Canaria Island (1560 km^2), good results are obtained with a 5866 nodes and 11683 triangles mesh.

On the other hand, the shadowing problem is a geometrical one. The approach to this issue should take into account the cast shadows by the complex orography in each time step, and the shadows cast by the clouds on the terrain.

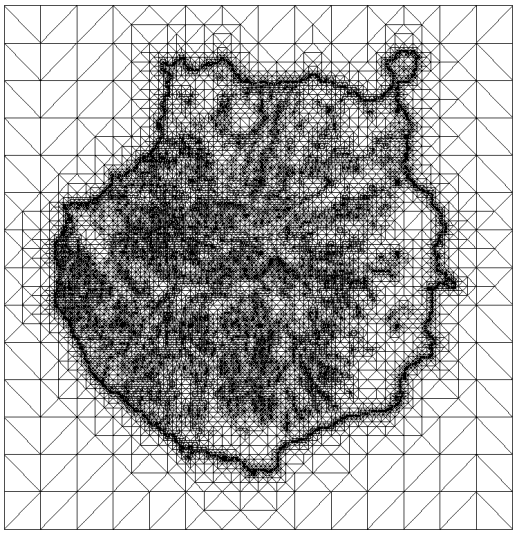

Fig. 10.1: Adaptive mesh for Gran Canaria Island

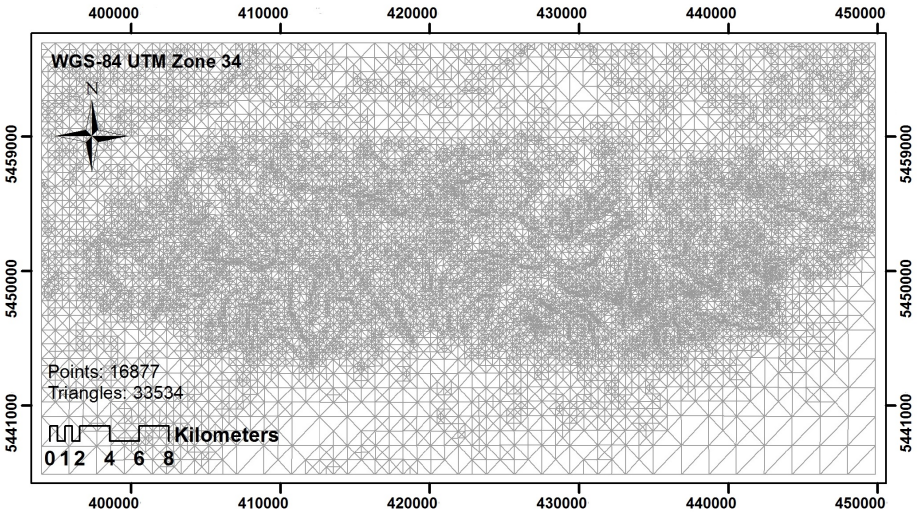

Fig. 10.2: Adaptive mesh for Tatra Mountains

10.2.2 Shadowing by orography

It is easy to think of a general technique to detect which triangles in the mesh are shadowed in an instant of time [16, 5]. A triangle will be under a cast shadow when,

looking at the mesh from the Sun, we can find a triangle that covers it. To do that, a reference system with the East in the x axis direction, and the North in the y axis direction (see Figure 10.3) is used. To determine the triangles that are behind another one, seen from the Sun, the reference system is changed to that of x', y' and z', with z' in the direction of the beam radiation. Now the domain mesh has to be projected on the $x'y'$ plane to find out which triangles are overlapped.

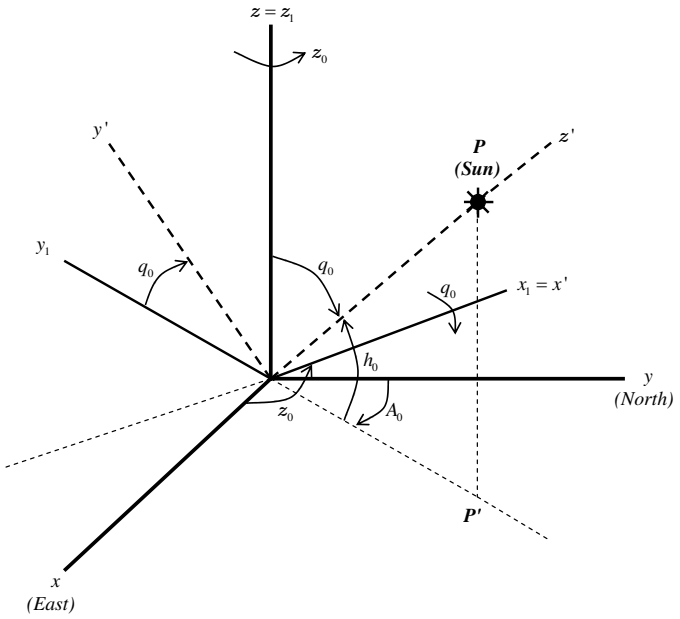

Fig. 10.3: Reference system

To build this reference system transformation, we need to know the position of the Sun respect to the Earth, for each time step. This function is named the solar vector, and has been studied by many authors [2, 28]. For every single time step, all the triangles need to be analyzed and assigned a shading level which is called the light factor, L_f, and that allows the user to diminish the solar radiation values in the shadowed triangle, according to the triangle proportion that is shadowed by other mesh elements. A triangle Δ has a light factor computed as:

$$L_f = \frac{n_{wp} - i}{n_{wp}} \tag{10.1}$$

with $i = 0, 1, \ldots, n_{wp}$ being the number of warning points inside other triangles that are in front of Δ. These *warning points* are the ones used to check which parts

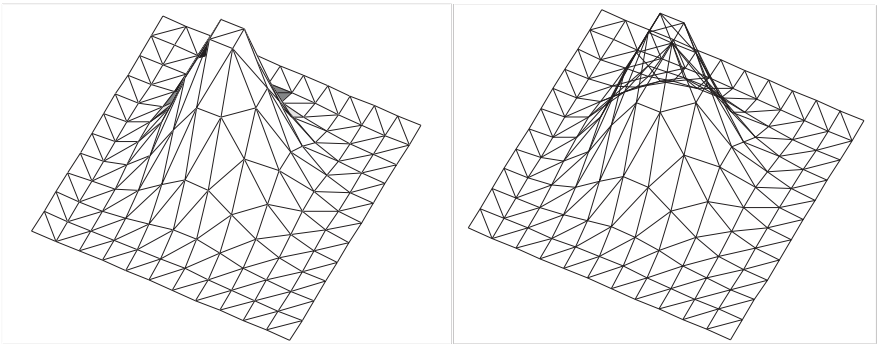

Fig. 10.4: Mesh from the Sun and projected one

of a triangle are shadowed. The factor will be applied to the estimation of diffuse and beam irradiance. To implement this procedure, a 4-T Rivara's refinement algorithm [25] is applied every time step to the intersected triangles (see Figure 10.5). The number of *warning points* depends upon the need of accuracy in the shadows determination process on the terrain.

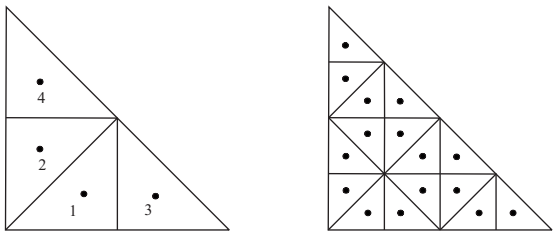

Fig. 10.5: Warning points

The presented procedure is simple and easy but, when the analyzed domain is big, the computational cost becomes unacceptable.

10.2.2.1 Triangles filtering process

Because of the above mentioned high computational cost, the need of a filtering process arises in order to choose the triangles which are likely to be shadowed and avoid the analysis on triangles that are impossible to be shaded. A triangle may be under shadows due to its own or self shadows, or due to the shadows cast by another one. When a surface is back to the Sun, it will be under its own or self shadows as

can be observed in Figure 10.6. A good way to compute this possibility is making use of the incidence angle[1] (δ_{exp}) as its value should be greater than $\pi/2$.

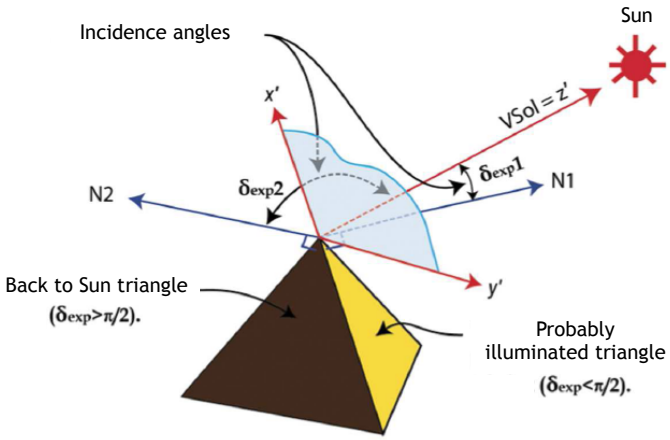

Fig. 10.6: Incidence angle and self shadows

This way, a *Self Shadows Light Factor* (L_{fss}) can be defined:

$$0 \quad \text{IF} \quad |\delta_{exp}| > (\pi/2) \tag{10.2}$$

$$1 \quad \text{IF} \quad (\pi/2) \geq |\delta_{exp}| \geq 0 \tag{10.3}$$

Now we are ready for the **first filtering** process, which means that the analysis on all *back to Sun* triangles can be avoided. A first conclusion can be done: only self shadowed triangles are able to cast shadows (see Figure 10.7), so they will be called *potential 1* triangles. Now the **second filtering** process begins projecting the mesh, referenced on the new plane $x' - y'$, towards z', forming parallelepipeds that we have called *cubes* (see Figure 10.8). Cubes depend on the studied time step, this is, the lower the Sun is, the more triangles will be included in one cube. At this stage, we need to remember that each triangle Δ needs to be analyzed to find other triangle(s) Δ' that intersects Δ and is before him respect to the Sun (coordinate z' of the intersection point is bigger for Δ' than for Δ).

Cubes are built in the plane $x' - y'$ in a way that the sides of their bases have to be equal or greater than the maximum value of the distance from the center to any of its nodes for all the grid triangles. So, the nodes of the mesh largest triangle do not extend beyond the eight parallelepipeds surrounding the cube which contains its center. Figure 10.9 shows the analysis of a time instant. Every *potential 1* triangle is associated to a cube containing its gravity center. When studying any of the illuminated triangles, the analysis is now limited to those *back to Sun* triangles placed

[1] Angle between the solar vector and the normal to a triangle surface

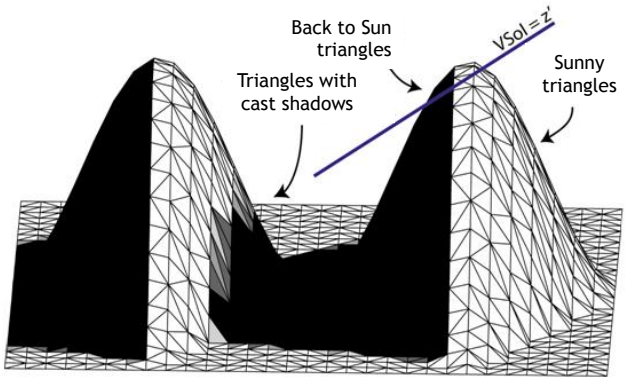

Fig. 10.7: Cast and self shadows

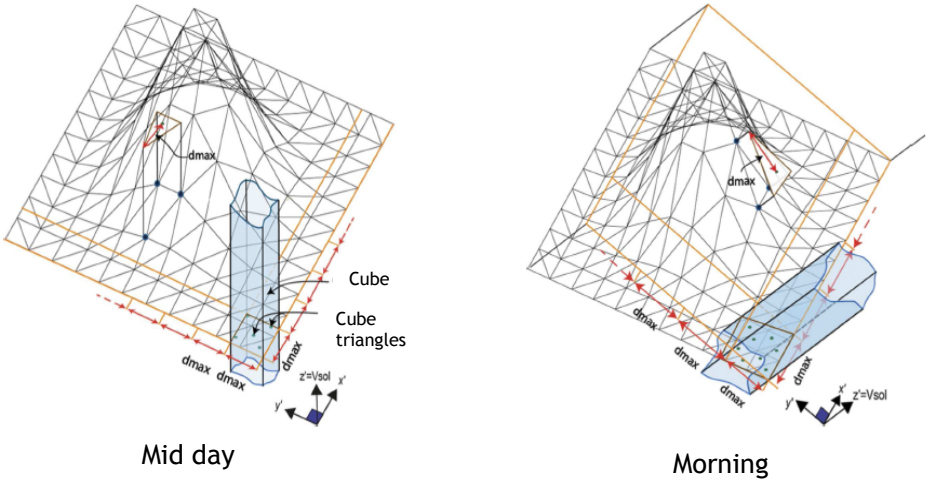

Fig. 10.8: 2^{nd} filtering: cubes

into those cubes which are around[2] them. At this stage, the *potential 2* triangles are defined as in Figure 10.9. So, now and for an illuminated triangle Δ, *potential 1* triangles far from our Δ, are discarded. What happens to *potential 2* triangles?. These ones and the analyzed illuminated triangle are embedded into cubic domains as shown in Figure 10.10. Now we can find *potential 2* triangles with cubic domains intersected with the domain of Δ, what will be called *potential 3* triangles (back to Sun, in close cubes, and with intersected domains), and other *potential 2* trian-

[2] the eight nearer cubes

gles, not intersected. These last ones are discarded too, making the **third filtering** process.

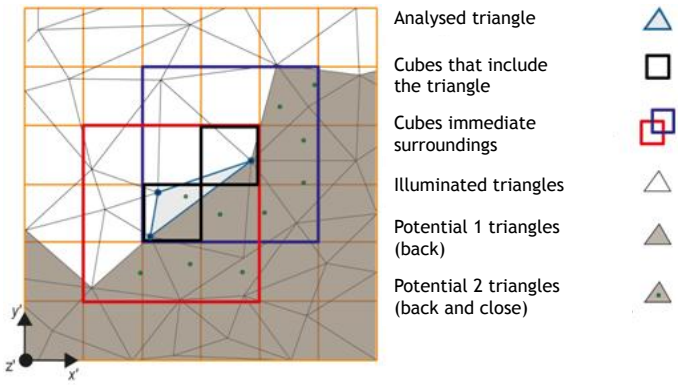

Fig. 10.9: Envelope and *potential 2* triangles

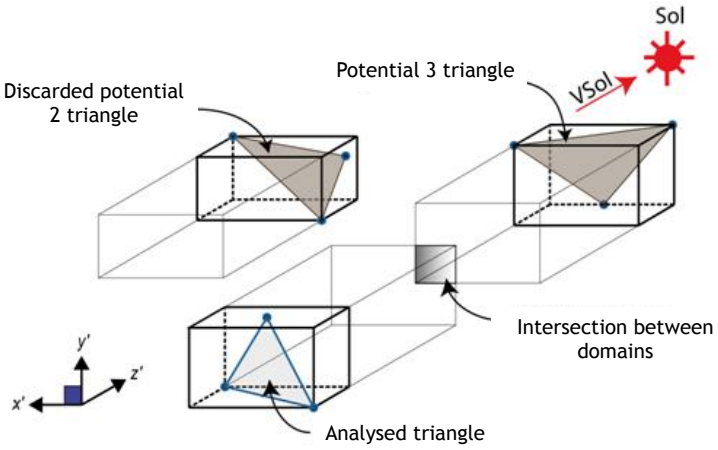

Fig. 10.10: Cubic domains

Now it is time to face the final decision on the quantity of shadowing that our illuminated triangle, Δ, has. As said above, the process is finished checking the projection of shadows on a small set of points, *warning points (wp)*. A *warning point* is shaded when (Figure 10.11):

1. The *warning point*, projected on the plane $x' - y'$, is into the projection of any *potential 3* triangle.
2. The *warning point* is farther from the Sun than point q in the potential triangle.

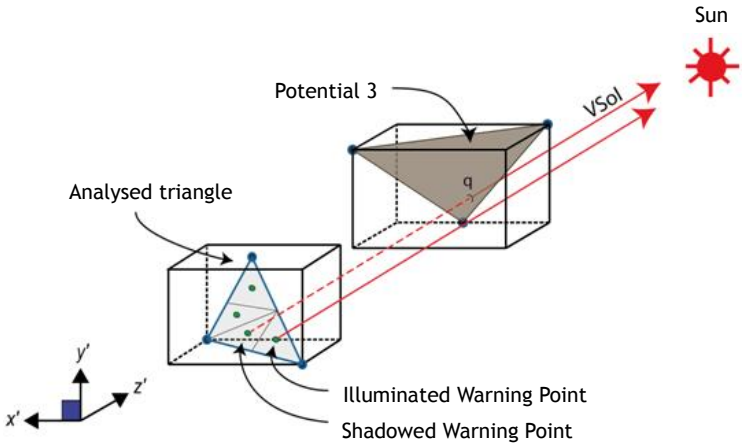

Fig. 10.11: Warning points analysis

Cast shadows *light factor*, L_{fcs} will be computed as above:

$$L_{fcs} = \frac{n_{wp} - i}{n_{wp}} \tag{10.4}$$

where $i = 0, 1, \ldots, n_{wp}$ is the number of *warning points* which are shaded, and n_{wp} the total number of *warning points*. Including the possibility of considering self shadows, the final *light factor*, L_f is

$$L_f = L_{fcs} \cdot L_{fss} \tag{10.5}$$

As examples, simulations on orographic shadows have been done on Gran Canaria and Tenerife islands (Canary Islands - Spain). Vectors (red or blue) in the Figures 10.12, 10.13 and 10.14, represent the solar vector direction for time and date of the simulation. As said above, the quantity of shadow is represented in a gray scale, from 0 to 1, according to the number of shaded *warning points* (L_f). See Figures 10.12, 10.13, and 10.14.

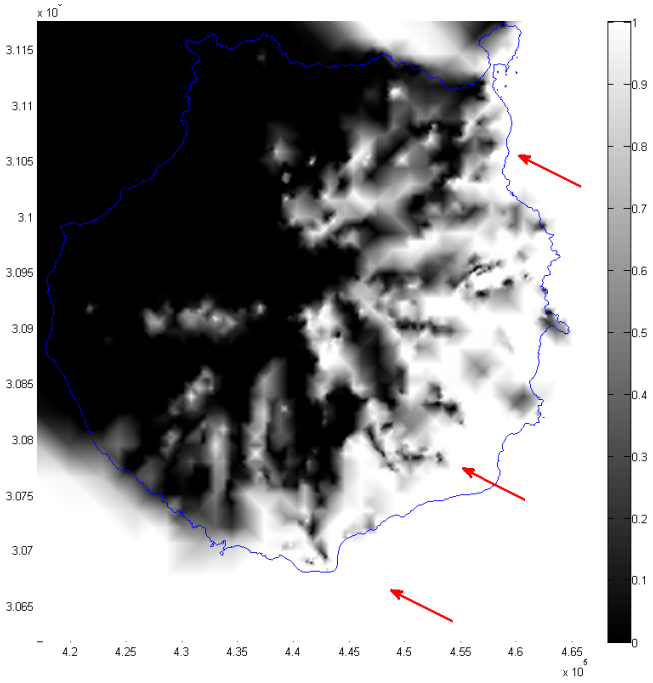

Fig. 10.12: Orographic shadows on Gran Canaria Island. January, 1st, 8:00 UTC

10.2.3 Shadowing by clouds

As we all know, clouds can cast shadows over the terrain and, considering their influence on the terrain is not an easy problem to solve because we do not know where and when clouds will be at any moment. Because of this, pictures of the actual clouds are interesting, what means that satellite images are a powerful tool for it. Statella and da Silva [29] or Fisher [9], are authors that have treated this issue. The Landsat dataset [35] is used in this chapter. Images come from sensors OLI and TIRS:

- Operational Land Imager (OLI)
- Thermal Infrared Sensor (TIRS) (bands 10 and 11)

OLI and TIRS sensors of the LANDSAT-8 images include 30 meters resolution nine spectral bands for bands 1-7 and 9. The panchromatic band (8), has a resolution of 15 meters. On the other hand, both thermal bands (10 and 11), are very interesting for surface temperatures, and have a resolution of 100 m. The Quality Control Band offers additional data, useful for determining the presence of snow, water or ice. Cirrus and clouds can be determined too with different levels of confidence. Starting from an image like the one in Figure 10.15, we will develop a cloud detection

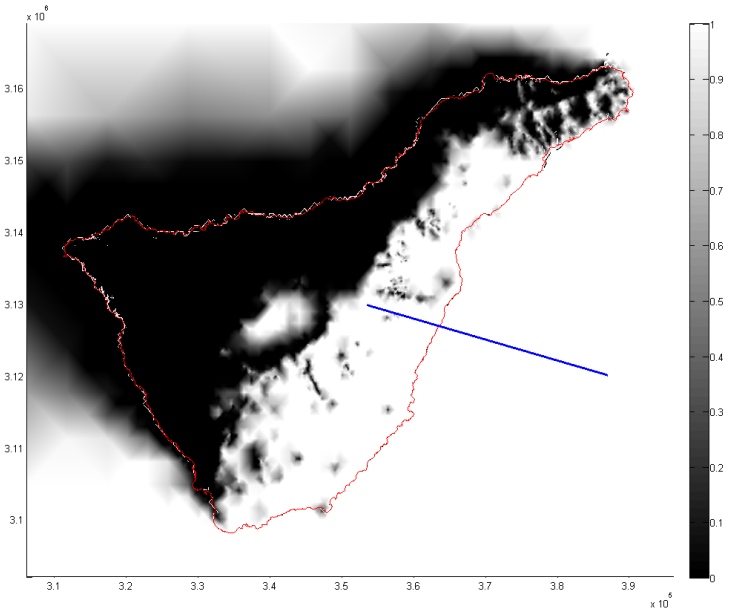

Fig. 10.13: Orographic shadows on Tenerife. February, 15th, 8:00 UTC

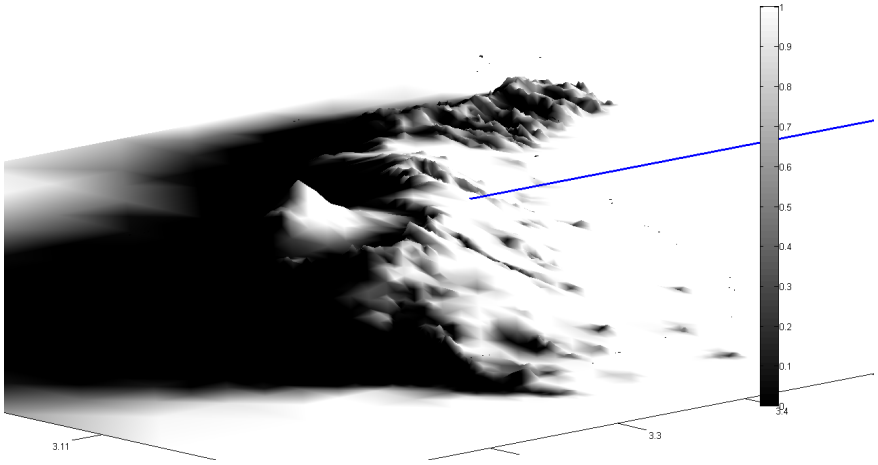

Fig. 10.14: 3D orographic shadows on Tenerife. February, 15th, 8:00 UTC

strategy based on the use of the satellite quality bands [34]. Assessing the shadows that come from clouds needs the estimate of radiance values from the image and the conversion of these ones into brightness temperature for, finally, computing the actual temperature that is used to assess clouds altitude and the shadow length (see Figure 10.16).

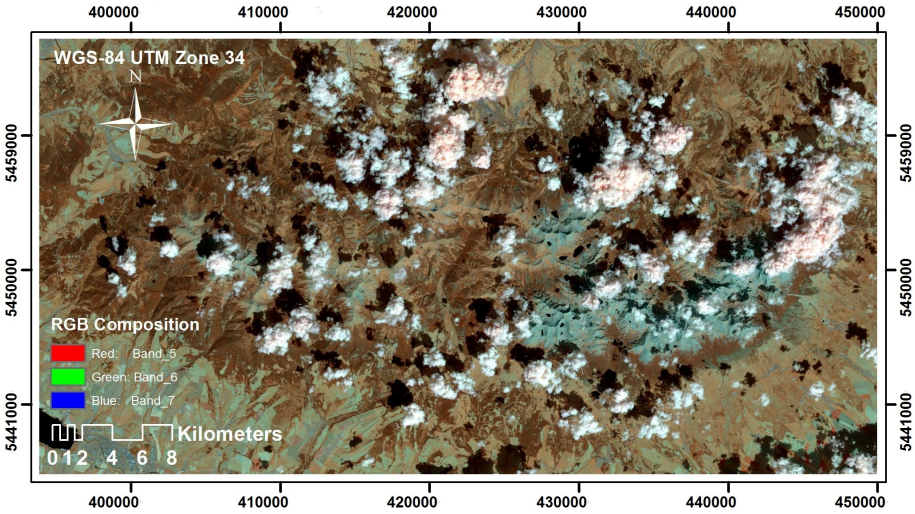

Fig. 10.15: RGB Composition on Tatra Mountains image. Bands 5, 6, 7.

According to [34], data from OLI and TIRS can be rescaled to the top of the atmosphere radiance values, using the equation 10.6.

$$L_\lambda = M_L \cdot Q_{cal} + A_L \tag{10.6}$$

where L_λ is the the top of the atmosphere (TOA) spectral radiance $(W/(m^2 \cdot srad \cdot um))$, M_L is the multiplicative scaling factor, A_L is the additive scaling factor, and Q_{cal} is the standard product quantified and calibrated pixel values.

Brightness temperature (K) [34], is calculated:

$$T_b = \frac{K_2}{\ln\left(\frac{K_1}{L_\lambda} + 1\right)} \tag{10.7}$$

T_b is the apparent brightness temperature (K), and K_1 and K_2 are specific conversion constants for bands 10 and 11. Real Land Surface Temperature is assessed through equation 10.8:

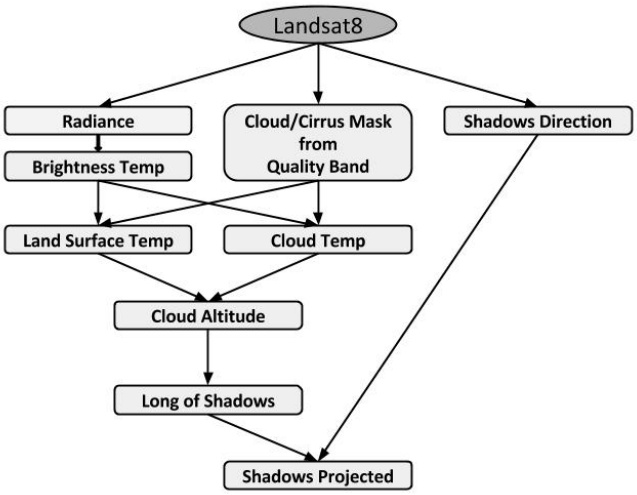

Fig. 10.16: Shadows from clouds flowchart.

$$T_s = c_0 + T_i + c_1 \cdot (T_i - T_j) + 2c_2 \cdot (T_i - T_j) + (c_3 + wc_4) \cdot (1 - \varepsilon) + (c_5 + wc_6) \cdot \Delta\varepsilon \tag{10.8}$$

with the coefficients computed according to [11, 24],

As indicated in [32, 10], Brightness Cloud Temperature obtained from thermal bands is assumed to be the Real Cloud Temperature. This way, the pixels group that makes a cloud, is assigned an average temperature to estimate its altitude, computed through Henning's formula (equation 10.9) [4].

$$H(m) = 125 \cdot (T - T_d) \tag{10.9}$$

where T is surface temperature and T_d is clouds temperature. Computing the shadows length (L) is easy [27, 20]:

$$L = \frac{H}{\tan h_0} \tag{10.10}$$

where h_0 is the elevation angle (see Figure 10.3).

The case of the Tatra Mountains (see Figure 10.15) is presented as an example of finding shadows on the terrain caused by clouds. We have used two shadow masks bands: number 10 and number 11, and finally chose number ten because of its better behaviour (see Figure 10.17).

Now it is time to move this mask into the mesh, and find what triangles are affected by shadows from clouds. Figure 10.18 shows our mesh with the new shadows. Light Factor for each triangle is computed using the above mentioned strategy of the *warning points*.

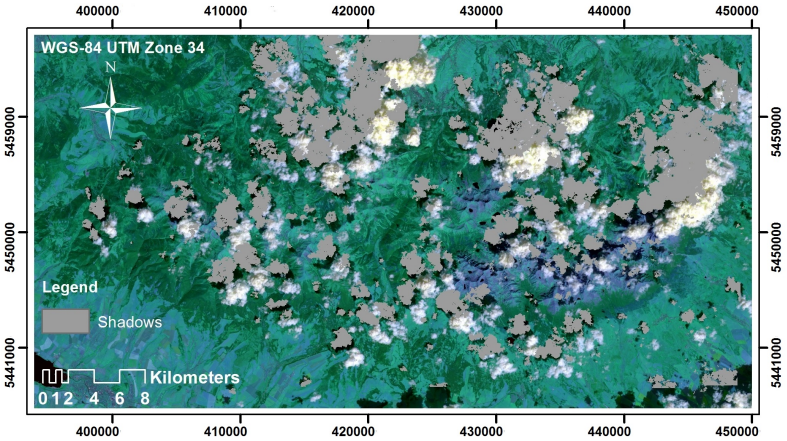

Fig. 10.17: Shadows mask. Band 10

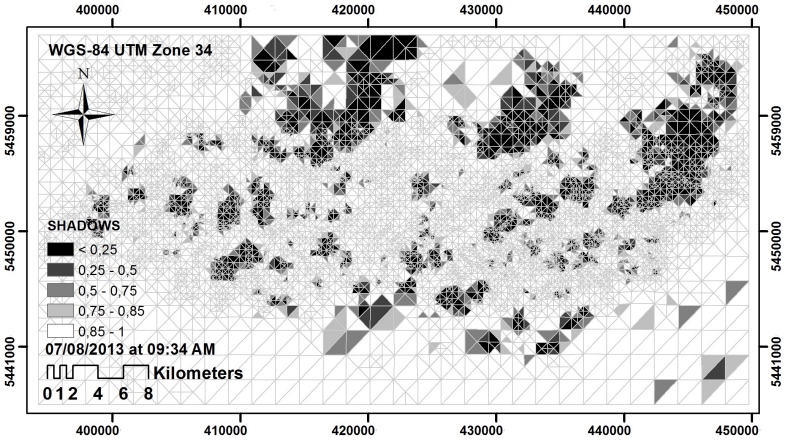

Fig. 10.18: Shadows estimation onto mesh

Drawing the actual shadows borderline with the estimation on the mesh (Figure 10.19), serves as a proof of how good is this approach that gives a good estimation for each time step with an affordable computational cost.

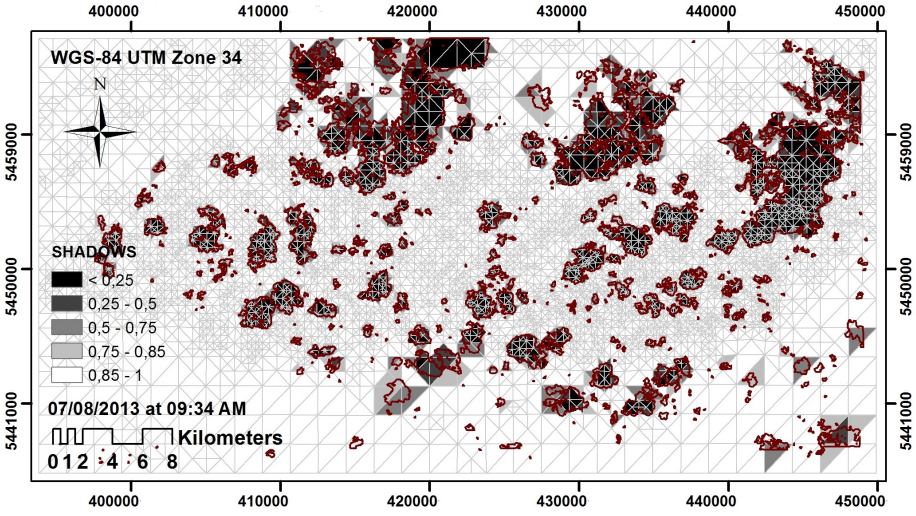

Fig. 10.19: Shadows borderline

10.3 Solar radiation model

In this approach, as we have the domain discretized through a triangles mesh, the solar radiation model constructed on the terrain grid needs to compute the solar radiation values on each triangle, for every time step. In short, the model explained here will be built on a clear sky radiation[3] model whose results will be corrected using a *clear sky index* (K_t^*)(equation 10.11) which takes into account all the measurements available for the analyzed domain. This way real sky radiation values can be obtained.

$$G = K_t^* \cdot G_c \tag{10.11}$$

where G is real sky radiation and G_c is clear sky radiation.

As we have some mathematical clear sky radiation models available (see Chapter 8), the actual problem to be solved is the computation of the conversion factor, this is, K_t^*. To get the radiation map of the studied domain, we need to do the following:

1. TMY calculation in the available measurement stations
2. Solar radiation calculation for all the mesh, assuming clear sky conditions
3. Calculation of K_t^* for all the mesh
4. Correction of clear sky solar radiation values using K_t^* to obtain real sky radiation

[3] Omitting cloud attenuation, clear sky radiation values are obtained

Of course, all steps are computed for each time step except step one which is done just once. Computation of K_t^* can be done for each time step, or for a considered time interval, let us say, a day, a month, etc.

In step one, a Typical Meteorological Year (TMY) is computed for all the available measurement stations in the domain. There are different approaches for determining this TMY, and the chosen one appears in [5, 15].

10.3.1 Clear sky solar radiation model

In this chapter, the ESRA [4] clear sky model is used [30, 31]. This model gives solar irradiance values in terms of their three components: *beam*, *diffuse* and *reflected* irradiances, being the global irradiance the addition of the three components. The beam irradiance is not scattered and reaches any surface directly with an associated direction. Diffuse irradiance is the scattered one. The reflected irradiance is the one reflected from one surface onto another. It depends on the ground albedo.

10.3.1.1 Beam radiation

The first step is computing the extraterrestrial irradiance G_0:

$$G_0 = I_0 \epsilon \tag{10.12}$$

where ϵ depends on the day angle, and the solar constant I_0 is 1367 (W/m^2) [22] The direct normal irradiance on earth surface in clear sky conditions, DNI_c (W/m^2), is attenuated by the cloudless atmosphere, and computed as:

$$DNI_c = G_0 \, exp\{-0.8662 T_{LK} m \delta_R(m)\} \tag{10.13}$$

The term $0.8662 T_{LK}$ is the corrected [12] dimensionless Linke atmospheric turbidity factor. The parameter m is the relative optical air mass [13], and $\delta_R(m)$ is the Rayleigh optical thickness at air mass m.

On a horizontal surface, the beam irradiance, of course for clear sky conditions $G_{bc}(0)$, is

$$G_{bc}(0) = (DNI_c) \cdot L_f \cdot \sin h_0 \tag{10.14}$$

where L_f is the light factor that takes into account the shadows (equation 10.5), and h_0 is the solar altitude angle. On an inclined surface, $G_{bc}(\beta)$ is

$$G_{bc}(\beta) = (DNI_c) \cdot L_f \cdot \cos \delta_{exp} \tag{10.15}$$

[4] European Solar Radiation Atlas

where δ_{exp} is the *solar incidence angle* measured between the characteristic vector of an inclined surface and the sun beam direction, and β is the angle between the inclined surface and the horizontal.

10.3.1.2 Diffuse radiation

On horizontal surfaces, this component is estimated with

$$DHI_c = G_{dc}(0) = G_0 T_n(T_{LK}) F_d(h_0) \tag{10.16}$$

It depends on the diffuse transmission T_n which depends on the Linke turbidity factor T_{LK}. Function F_d, in turn, depends on the solar altitude h_0 [26]. On a inclined surface, $G_{dc}(\beta)$, both, sunlit and shadowed surfaces have to be considered as in [18].

10.3.1.3 Reflected radiation

According to [19], the ground reflected irradiance $G_r(\beta)$ is computed as

$$G_r(\beta) = \rho_g GHI_c r_g(\beta) \tag{10.17}$$

where

$$r_g(\beta) = \frac{(1-\cos\beta)}{2} \tag{10.18}$$

$$GHIc = G_{bc}(0) + DHIc \tag{10.19}$$

being ρ_g the mean ground albedo and $r_g(\beta)$ the fraction of ground viewed by an inclined surface.

10.3.2 Computing the clear sky index. Real sky solar radiation model

At this stage, irradiance values in clear sky conditions have been obtained. However, it is obvious that real sky conditions, considering the clouds, are the actual goal. To reach these real sky radiation values, the clear sky index (see equation 10.11), is very useful. Now it depends upon the available measurement data to compute the K_t^*. If we have instantaneous irradiance measurements in any station, we will have instantaneous clear sky indexes for that station (s) at any time step (i) as seen in equation 10.20.

$$K^*_{t_{s,i}} = \frac{G_s}{G_{c,s}} \tag{10.20}$$

But sometimes the available data in a measurement station is irradiation (H_s) along a time period. In this case, clear sky index for a station (s) and for that time period, is obtained this way:

$$K_{t_s}^* = \frac{H_s}{H_{c,s}} = \frac{H_s(0)}{H_{c,s}(0)} \tag{10.21}$$

where

$$H_{c,s}(0) = \int_0^T G_{c,s}(0)\,dt \tag{10.22}$$

As measurement equipments usually work on a horizontal plane ($\beta = 0$), computing $K_{t_s}^*$ will be as in 10.21. All these clear indexes are those computed for any of the available measurement stations in the domain. Of course, any computed $K_{t_s}^*$ is for the triangle where the measures were taken. But in the domain we will have hundreds of triangles with no measures. In these ones, an interpolation procedure is implemented to estimate the value ok K_t^*. A formula for complex orography [17] is applied,

$$K_t^* = \varepsilon \frac{\sum_{n=1}^{N} \frac{K_{tn}^*}{d_n^2}}{\sum_{n=1}^{N} \frac{1}{d_n^2}} + (1-\varepsilon) \frac{\sum_{n=1}^{N} \frac{K_{tn}^*}{|\Delta h_n|}}{\sum_{n=1}^{N} \frac{1}{|\Delta h_n|}} \tag{10.23}$$

where K_t^* is the clear sky index at each mesh triangle, K_{tn}^* is the clear sky index at measurement stations, d_n is the horizontal distance and $|\Delta h_n|$ is the altitude difference between station n and the studied point, N is the number of stations in the interpolation, and ε is a fitting parameter between 0 and 1. Of course, equation (10.23) continuity is guaranteed assuming the measured values at the stations.

Now, for any triangle of the mesh, irradiance in real sky conditions is easily computed as follows,

$$GHI = G(0) = K_t^* \cdot GHI_c \tag{10.24}$$

As a summary, an outline of the process is presented in Figure 10.20

10.4 Numerical experiments. Solar maps

Talking about solar radiation maps is usually talking about irradiation distribution on a terrain. As an example, several numerical experiments in some of the Canary Islands are presented. The Canary Islands is an archipelago of seven islands placed in the northwestern part of Africa, in a latitude around 28, with a subtropical climate. In fact, we have already seen some shadowing examples for Tenerife and Gran Canaria Island. Figure 10.21 shows the Gran Canaria Island elevation map, with all the measurements stations available (see characteristics in Table 10.1).

Firstly, the correct determination of the ε parameter in equation 10.23 is sought. For that, it is necessary a good knowledge about the climate conditions of the do-

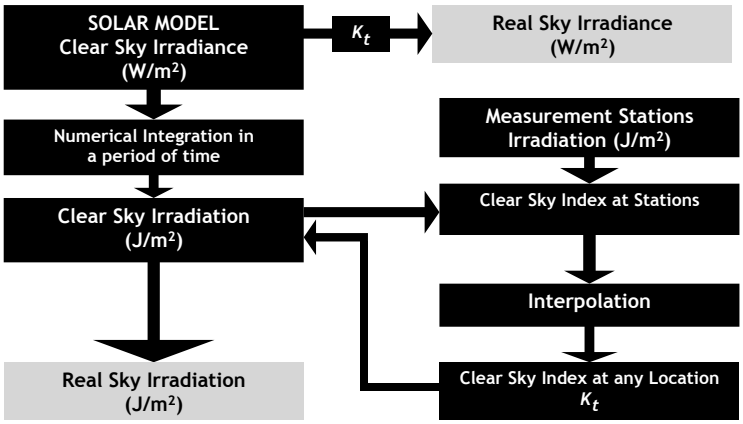

Fig. 10.20: Solar radiation model

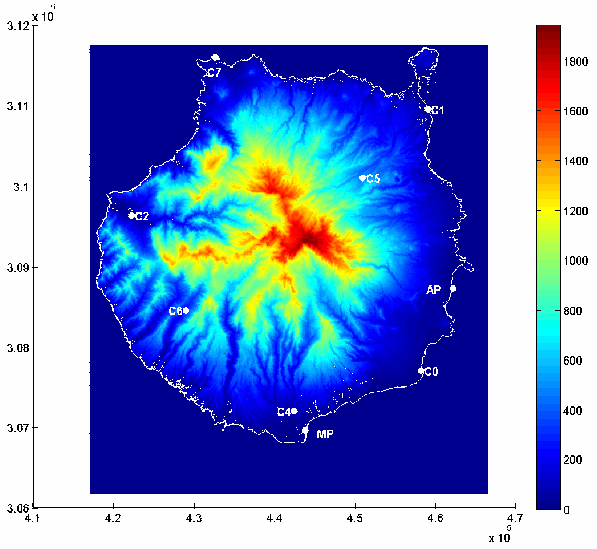

Fig. 10.21: Gran Canaria Island elevation map

main, this is, of the zone under study. In this case, the Canary Islands are under the influence of the Trade Winds which come from the Northeast full of humidity, and that get stopped by the mountains of the islands producing a different behaviour between the northeast and the southwest of the isles. Varying ε, we obtain a K_t^* distribution map for January and July (see Figure 10.22 and Figure 10.23).

Table 10.1: Available measurement stations in Gran Canaria Island.

Station	label	latitude	longitude	altitude
Pozo Izquierdo	C0	27.8175 N	15.4244 W	47
Las Palmas de G. C.	C1	28.1108 N	15.4169 W	17
La Aldea de San Nicolás	C2	27.9901 N	15.7907 W	197
San Fernando de M.	C4	27.7716 N	15.5841 W	265
Santa Brígida	C5	28.0337 N	15.4991 W	525
Mogán (village)	C6	27.8839 N	15.7216 W	300
Sardina de Gáldar	C7	28.1681 N	15.6865 W	40

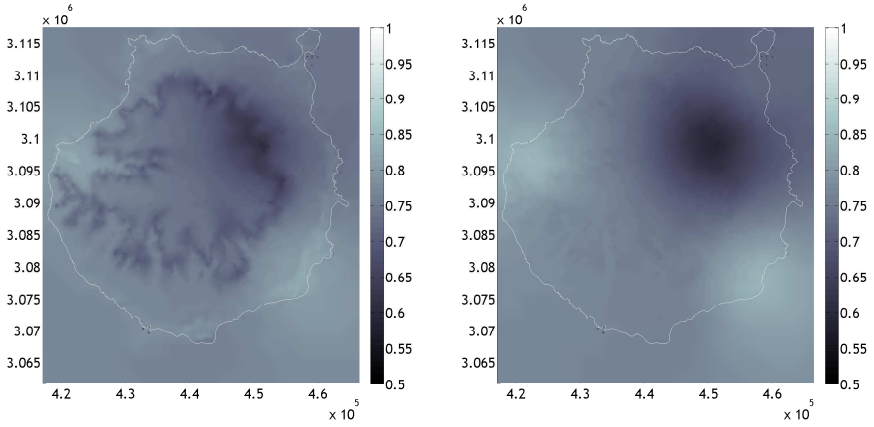

Fig. 10.22: K_t^* distribution for January. $\varepsilon = 0.5$ and $\varepsilon = 0.9$

Both figures show a false behaviour of K_t^* with $\varepsilon = 0.5$, while with that parameter equal to 0.9, the behaviour of the clouds fits what is known about the Canary Islands climate. This means that clouds depend on the horizontal displacements on the domain, more than on the vertical ones. With this ε, we compute K_t^* in all the triangles, and obtain the real sky irradiance as a correction of the clear sky one. To complete the maps, it is only needed to integrate the irradiance in all the domain, along a time period, and represent it. As an example, Figures 10.24 and 10.25 show a monthly average irradiation map for all the clear sky components in a TMY January. It is really interesting to watch the influence of K_t^* comparing pictures in Figure 10.26. The first one presents the clear sky irradiation map for TMY July, and the second one is the real sky irradiation map for the same month. This is a month with an important influence of the Trade Winds, that can be observed in the north and northeast side of the island, with lower irradiation values than on the south face.

It can be clearly observed that cloudiness and orographic shadows have been taken into account. To observe better this fact, Figure 10.26 is presented, with a three

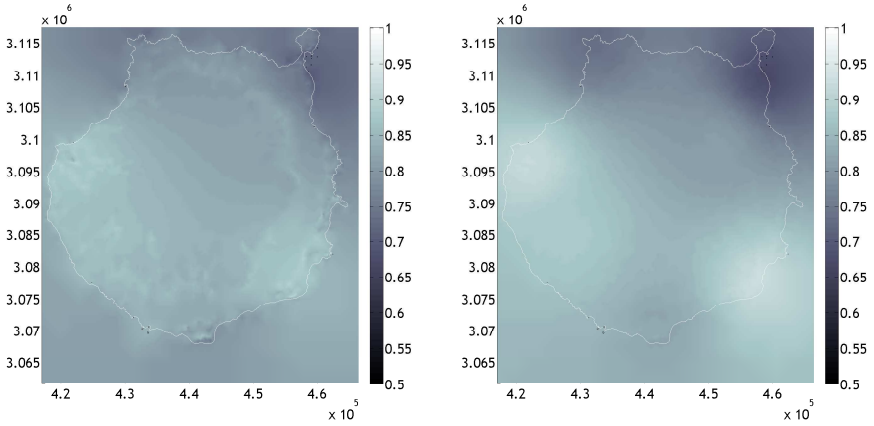

Fig. 10.23: K_t^* distribution for July. $\varepsilon = 0.5$ and $\varepsilon = 0.9$

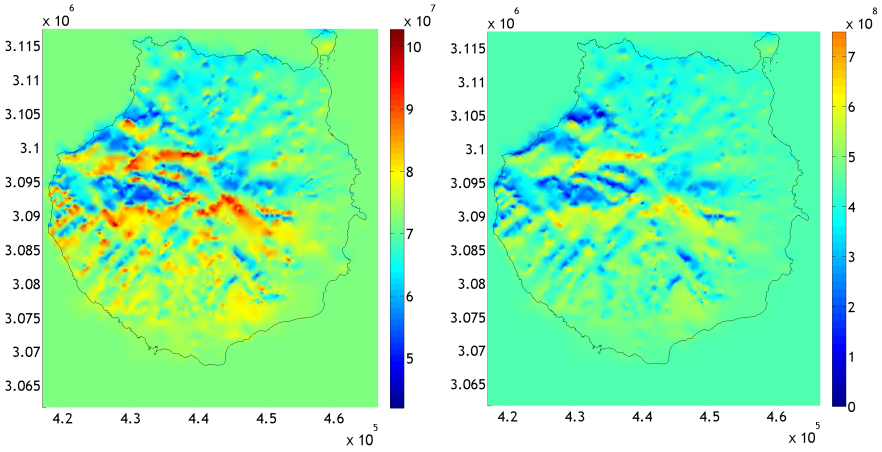

Fig. 10.24: Clear sky irradiation (J/m^2) maps for Gran Canaria in January. Diffuse and Beam

dimensional view of the island irradiation map. Please note that relation between vertical and horizontal scales have been exaggerated.

The morphology of this island (Gran Canaria) is very radial so, this is an advantage to apply equation 10.23. Moreover, it works perfectly when applying to other islands with more complex orography and with a morphology quite different from the radial one. As an example, numerical experiments in Tenerife Island are presented in Figure 10.28.

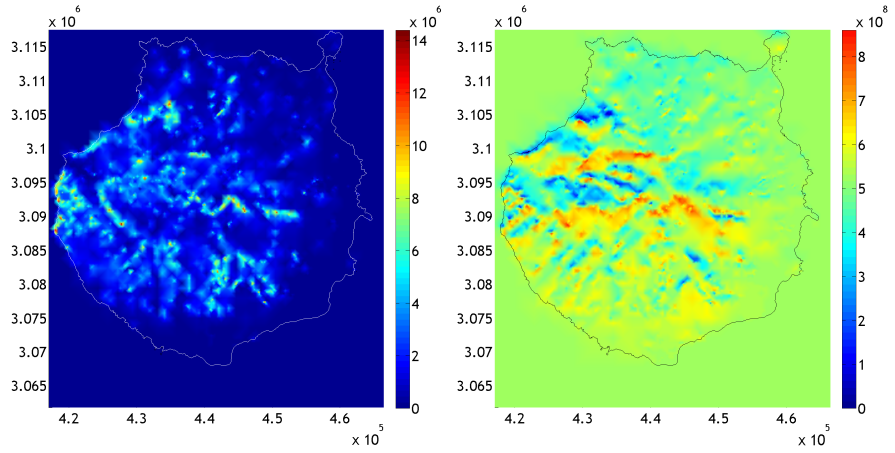

Fig. 10.25: Clear sky irradiation (J/m^2) maps for Gran Canaria in January. Reflected and Global

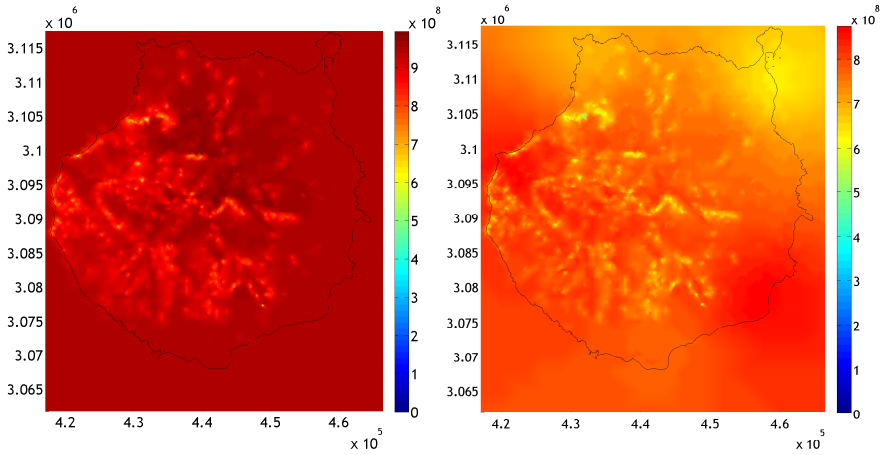

Fig. 10.26: Clear and real sky irradiation (J/m^2) maps for Gran Canaria in July

10.5 Constructing predictive solar maps

In previous sections, how to build a solar map using punctual ground solar radiation measurements has been explained. This procedure results in a characterization of the domain (i.e., an island), which is very helpful to understand the solar radiation behaviour for agronomic, biological or engineering purposes. In this last aspect, electrical energy production highlights. Regarding to this, power systems stability and planning need a great knowledge about the future electrical production of the

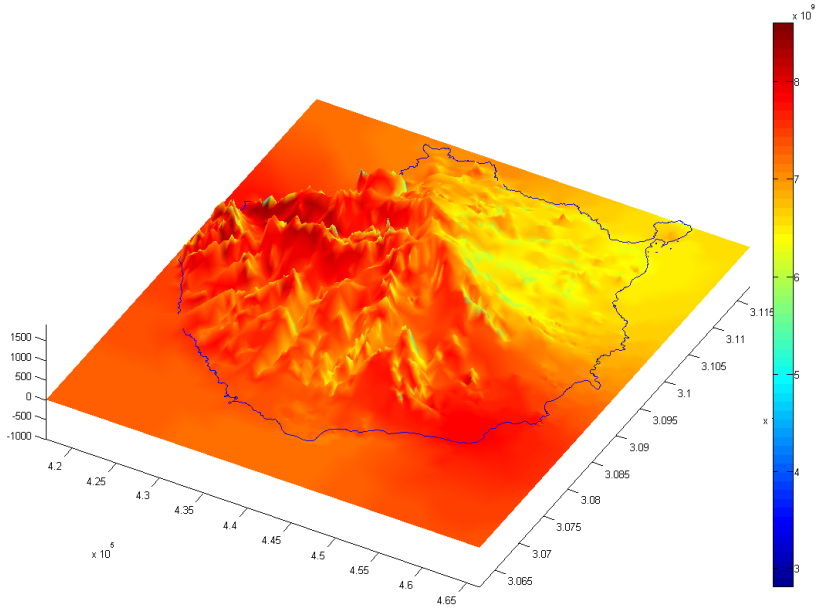

Fig. 10.27: 3D real sky annual irradiation map for Gran Canaria Island

different generators involved in the grid. So, if there are big solar power facilities injecting energy, an efficient and accurate prediction tool for solar radiation is needed. Because of this we have presented some solar radiation prediction tools in this book (see Chapters 8 and 9).

In this section we will convert our solar maps generation code in a prediction tool [7], making use of a Numerical Weather Prediction (NWP) model like Harmonie, ECMWF or other. In this example, model MM5[5] is used. The methodology applied is the one explained in this chapter but, using MM5 predicted data instead of the TMY measurement stations data. This NWP model assesses irradiances on a grid whose horizontal projection is not uniform. These data have to be transported to our adaptive mesh interpolating the results to the centres of the triangles.

We have to adapt our model according to the NWP used. In example, MM5 does not take into account the actual domain orography, nor the casting of shadows. On the other hand, as said above, determining the clear sky index for every node in the MM5 grid (transposed to the mesh) is needed. As the NWP grid changes their values depending on time, we will have to use a clear sky index for each node and time step ($K_{t_i}^*$).

[5] National Center for Atmospheric Research (Pennsylvania State University -USA-) mesoscale fifth generation model

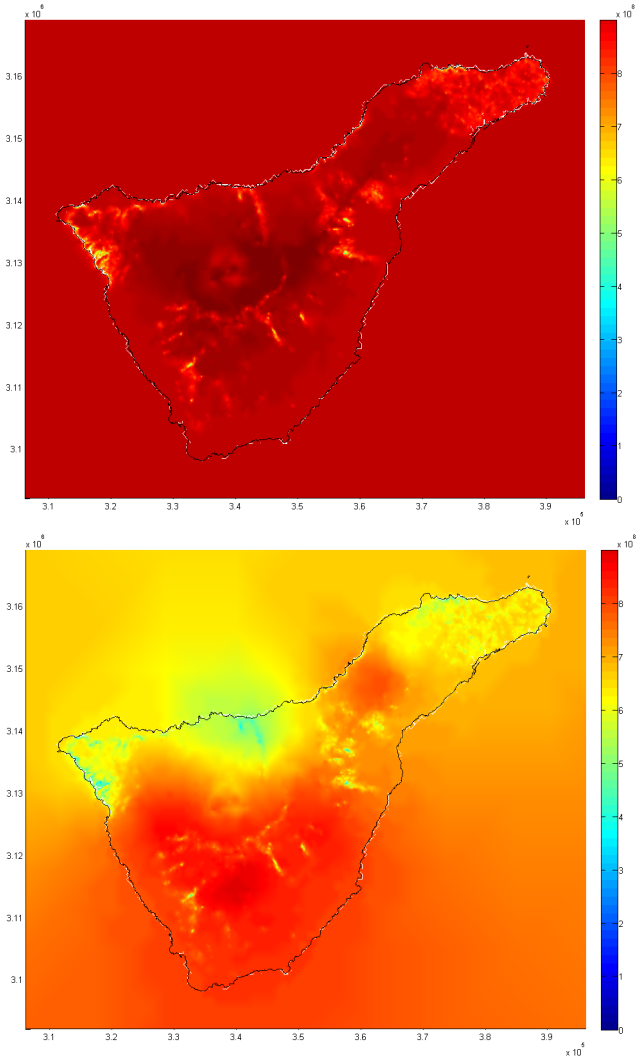

Fig. 10.28: Clear and real sky irradiation (J/m^2) maps for Tenerife Island in July

$$K_{t_i}^* = \frac{G(0)}{G_{c_{ss}}(0)} \tag{10.25}$$

where $G_{c_{ss}}(0)$ is the horizontal clear sky irradiance, considering only self shadows. Later, the final real sky predicted irradiance will be computed using this $K_{t_i}^*$ and $G_c(0)$ considering the self and cast shadows. Computing the clear sky index includes these steps:

1. Make an MM5 grid triangulation where the nodes are those from the MM5 grid, and are assigned the predicted radiation for every time step
2. The new MM5 triangulated grid overlaps the orography adaptive mesh. If we take a look at Figure 10.29, we can see that every orography triangles are assigned the interpolated irradiance using equation (10.26)

$$\begin{bmatrix} x \\ y \\ z \end{bmatrix} = \begin{bmatrix} x_0 \\ y_0 \\ z_0 \end{bmatrix} + K_1 \cdot \begin{bmatrix} V_{1_x} \\ V_{1_y} \\ V_{1_z} \end{bmatrix} + K_2 \cdot \begin{bmatrix} V_{2_x} \\ V_{2_y} \\ V_{2_z} \end{bmatrix} \tag{10.26}$$

   Three equations in three unknowns, K_1, K_2 and z, that is the predicted irradiance for the adaptive mesh triangle
3. Clear sky index ($K^*_{t_i}$) is computed for each triangle and time step, using self shadows clear sky irradiance

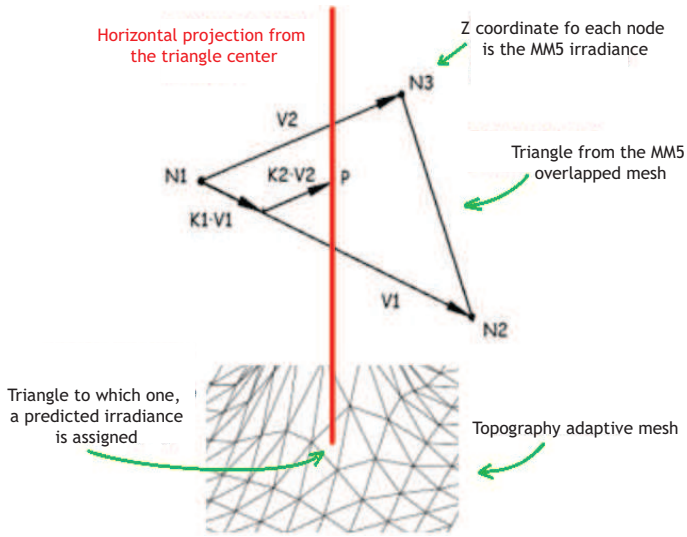

Fig. 10.29: Predicted irradiance transpose to mesh

Computing $K^*_{t_i}$ will be done with equation 10.23 for each and every triangle of the mesh, and for every time step. As a summary, Figure 10.30 shows an outline of the procedure to follow, where measurements have been substituted by predictions in the determination of $K^*_{t_i}$.

A numerical simulation using this methodology is done in two locations of Gran Canaria: *Temisas*[6] and *Lomo Carbonero*[7]. As the clear sky index is computed for

[6] 27.917°N 15.491°W

[7] 28.033°N 15.533°W

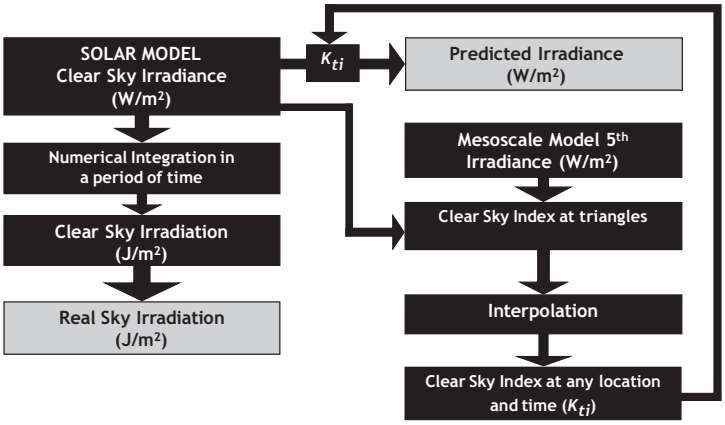

Fig. 10.30: Predictive solar radiation model

each time step, the daily cloudiness evolution can be addressed through this parameter (see Figure 10.31). Starting from this distribution, the predicted irradiance for every time step can be computed (see Figure 10.32).

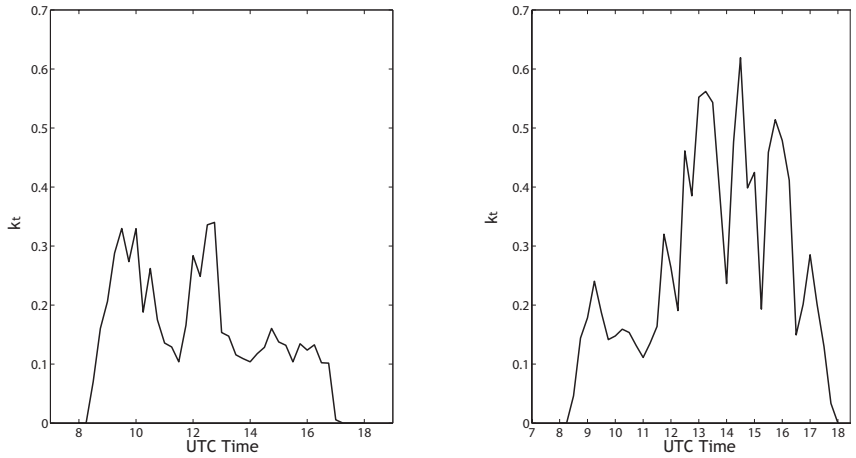

Fig. 10.31: Clear sky index prediction for *Temisas* and *Lomo Carbonero*

The example has been done for different locations in the domain. If we compute it for all the triangles and for one instant, we will obtain an irradiance predicted map and, for different time steps, we will get a family of maps with the predicted

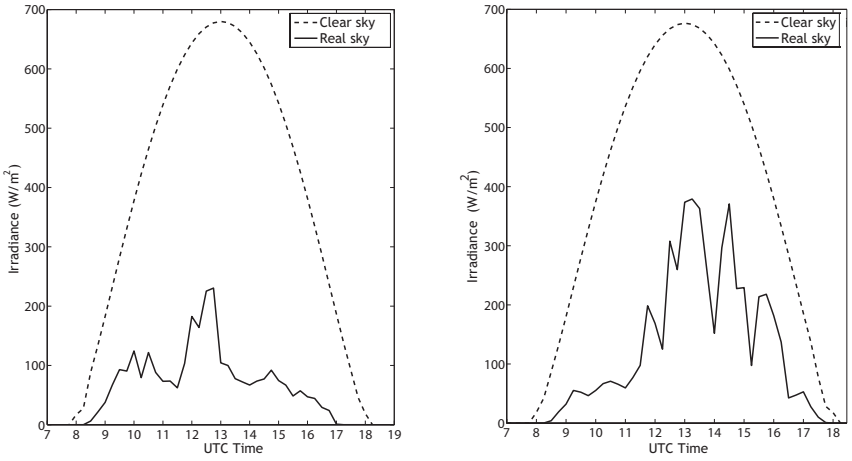

Fig. 10.32: *Temisas* and *Lomo Carbonero* horizontal predicted irradiance

evolution of the irradiance. In case that daily (or monthly,...) irradiation values are needed, integration of the predicted irradiance will have to be previously performed.

10.6 Conclusions

This chapter is devoted to the explanation of the methodology used in making solar maps. These maps are usually done with monthly or annual irradiation values but sometimes it is interesting to have irradiance maps, especially when we are talking about solar radiation predictions. The discretization of the complex terrain orography has been done using adaptive triangular meshes which allow to build surfaces that cast shadows. Moreover, this method is more efficient from the computational point of view when compared to the use of digital elevation maps or uniform meshes.

Values for real sky conditions are obtained from those computed using a clear sky solar radiation model, affected by the clear sky index. This one is valid for a triangle and a time step. The key issue, therefore, is computing $K_{t_i}^*$. A TMY is very useful to get monthly or annual solar irradiation maps.

References

1. A. Ångstrom.: Solar and terrestrial radiation. Monthly Weather Review **52**, 397 (1924)
2. M. Blanco-Muriel, D.C. Alarcón-Padilla, T. López-Moratalla, M. Lara-Coira.: Computing the solar vector. Solar Energy **70**, 431–441 (2001)

3. E. Cogliani, P. Ricchiazzi.: Generation of operational maps of global solar irradiation on horizontal plan and of direct normal irradiation from Meteosat imagery by using SOLARMET. Solar Energy **82**, 556–562 (2008)
4. T. Chiyu, H. Kon, C. Magono.: The Cloud-base Topography and Formation Condition of Cumulus Humilis Clouds. Journal of the Faculty of Science, Hokkaido University. Series 7, Geophysics **4** (1), 43–57 (1972)
5. F. Díaz, G. Montero, J.M. Escobar, E. Rodríguez, R. Montenegro.: An Adaptive Solar Radiation Numerical Model. Journal of Computational and Applied Mathematics **236**, 4611–4622 (2012)
6. F. Díaz, H. Montero, D. Santana, G. Montero, E. Rodríguez, L. Mazorra Aguiar, A. Oliver.: Improving shadows detection for solar radiation numerical models. Applied Mathematics and Computation **319**, 71–85 (2018)
7. F. Díaz, G. Montero, J.M. Escobar, E. Rodríguez, R. Montenegro.: A new predictive solar radiation numerical model. Applied Mathematics and Computation **267**, 596–603 (2015)
8. J. Dozier, J. Bruno, P. Downey.: A faster solution to the horizon problem. Computers & Geosciences **7**, 145–151 (1981)
9. A. Fisher.: Cloud and Cloud-Shadow Detection in SPOT5 HRG Imagery with Automated Morphological Feature Extraction. Remote Sensing **6**, 776–800 (2014)
10. T. Inoue.: On the temperature and effective emissivity determination of semi-transparent cirrus clouds by Bi-Spectral measurements in the 10nm window region. Journal of the Meteorological Society of Japan **63** (1), 88–99 (1984)
11. J.C. Jiménez-Muñoz, J.A. Sobrino, D. Skokovic, C. Mattat, J. Cristóbal.: Land Surface Temperature Retrieval Methods From Landsat-8 Thermal Infrared Sensor Data. IEEE Geoscience and remote sensing letters **11** (10), 1840–1843 (2014)
12. F. Kasten.: The Linke turbidity factor based on improved values of the integral Rayleigh optical thickness. Solar Energy **56** (3), 239–244 (1996)
13. F. Kasten, A.T. Young.: Revised optical air mass tables and approximation formula. Applied Optics **28**, 4735–4738 (1989)
14. B.Y.H. Liu, R.C. Jordan.: The Long-Term Average Performance of Flat-Plate Solar Energy Collectors. Solar Energy **7**, 53–74 (1963)
15. L. Mazorra, F. Díaz, G. Montero, R. Montenegro.: Typical meteorological year (TMY) evaluation for power generation in Gran Canaria Island, Spain. In: Proceedings of 25^{th} European Photovoltaic Solar Energy Conference and Exhibition, Valencia, Spain, 4726–4728 (2010)
16. G. Montero, J.M. Escobar, E. Rodríguez, R. Montenegro.: Solar radiation and shadow modelling with adaptive triangular meshes. Solar Energy **83**, 998–1012 (2009)
17. G. Montero, R. Montenegro, J.M. Escobar.: A 3-D Diagnostic Model for Wind Field Adjustment. J Wind Engrg Ind Aer **74-76**, 249–7261 (1998)
18. T. Muneer.: Solar Radiation model for Europe. Building Services Engineering Research and Technology **11**, 153–163 (1990)
19. T. Muneer.: Solar Radiation and Daylight Models for Energy Efficient Design of Buildings. Architectural Press, Oxford (1997)
20. J.P. Musial, F. Husler, M. Sutterlin, C. Neuhaus, S. Wunderle.: Probabilistic approach to cloud and snow detection on Advanced Very High Resolution Radiometer (AVHRR) imagery. Atmos. Meas. Tech. **7**, 799–822 (2014)
21. A. Niewienda, F.D. Heidt.: SOMBRERO: a PC-tool to calculate shadows on arbitrarily oriented sufaces. Solar Energy **58**, 253–263 (1996)
22. J.K. Page (ed).: Prediction of Solar Radiation on Inclined Surfaces'. D. Reidel Publishing Co., Dordrecht (1986)
23. R. Perez, R. Seals, P. Ineichen, R. Stewart, D. Menicucci.i.: A new simplified version of the perez diffuse irradiance model for tilted surfaces. Solar Energy **39**, 221–231 (1987)
24. A. Rajeshwari, N.D. Mani.: Estimation of land surface temperature of Dindigul district using Landsat 8 data. International Journal of Research in Engineering and Technology **3** (5), 122–126, (2014)
25. M.C. Rivara.: A Grid Generator Based on 4-Triangles Conforming. Mesh-Refinement Algorithms. Int J Num Meth Engrg **24**, 1343–1354 (1987)

26. K. Scharmer, J. Greif.: The European Solar Radiation Atlas.Vol. 2 : Database and exploitation software. Les Presses de l'Ecole des Mines, Paris (2000)
27. J.J. Simpson, J.R. Stitt.: A procedure for the detection and removal of cloud shadow from AVHRR data over land. IEEE Transactions on Geoscience and Remote Sensing **36** (3), 880–897 (1998)
28. A.B. Sproul.: Derivation of the solar geometric relationships using vector analysis. Renewable Energy **32**, 1187–1205 (2007)
29. T. Statella, E.A. da Silva.: Shadows and clouds detection in high resolution images using mathematical morphology. In: Proceedings of Pecora 17 Conference The Future of Land Imaging...Going Operational, Denver, USA (2008)
30. M. Šúri, J. Hofierka.: A New GIS-based Solar Radiation Model and its application to photovoltaic assessments. Transactions in GIS **8**, 175–170 (2004)
31. M. Šúri, J. Hofierka.: The solar radiation model for Open source GIS: implementation and applications. In: Benciolini, B., Ciolli, M., Zatelli, P. (Eds.), Proceedings of the Open source GIS-GRASS users conference, Trento, Italy, 1–19 (2002)
32. C.R. Yost, P. Minnis, S. Sun-Mack, Y. Chen, M. McGill.: Use of active remote sensors to improve the accuracy of cloud top heights derived from thermal satellite observations. In: Proc. AMS Symp. Recent Developments in Atmos. Appl. Radar & Lidar, New Orleans, USA (2008)
33. K. Zakšek, T. Podobnikar, K. Oštir.: Solar radiation modelling. Computers & Geosciences **31**, 233–170 (2005)
34. K. Zanter (ed).: LANDSAT-8 (L8) data users handbook. Department of the Interior U.S. Geological Survey, Maryland-USA (2016)
35. Z. Zhu, C.E. Woodcock.: Object-based cloud and cloud shadow detection in Landsat imagery. Remote Sensing of Environment —textbf118, 83–94 (2012)